Official Publication Statement:
This paper has been formally published as:
Title: Performance evaluation of S-PET, a compact, LYSO/BGO phoswich detector small animal PET prototype,
Journal: *Physics in Medicine and Biology*,
DOI: 10.1088/1361-6560/ae4b02,
URL: https://iopscience.iop.org/article/10.1088/1361-6560/ae4b02.
This preprint is the preliminary version. Please cite and refer to the published journal article as the definitive version.

Performance evaluation of S-PET, a compact, high sensitivity and high resolution small animal PET prototype

Hang Yang[1,2,†] , Wen He[1,4,†], Xin Zhao[1,5], Guangming Li[1,6], Yangyang Zhao[1,7], Wenjie Huang[1], Yong Huang[3], Ming Niu[1], Ying Liang[3], Zheng Gu[1,*]

[1] Institute of Biomedical Engineering, Shenzhen Bay Laboratory, Shenzhen, China.
[2] School of Astronautics, Harbin Institute of Technology, Harbin, China.
[3] Department of Nuclear Medicine, National Cancer Center/National Clinical Research Center for Cancer/Cancer Hospital & Shenzhen Hospital, Chinese Academy of Medical Sciences and Peking Union Medical College, Shenzhen, 518116, China.
[4] Department of Radiology, Stanford University, Stanford, CA, USA.
[5] Institute of Medical Technology, Peking University Health Science Center, Peking University, Beijing, China.
[6] School of Sciences, Beijing University of Posts and Telecommunications, Beijing, China.
[7] University of Science and Technology Beijing, Beijing Engineering Research Center of Industrial Spectrum Imaging, School of Automation and Electrical Engineering, Beijing, China.
† These authors contribute equally to this work.
∗ Corresponding author.

E-mail: guzheng@szbl.ac.cn

Abstract. S-PET is a compact, high sensitivity and high resolution small animal PET prototype developed at Shenzhen Bay Laboratory (SZBL). The S-PET system employs a phoswich depth of interaction (DOI) detector design, which also allows identification of the large majority of the cross layer crystal scatter (CLCS) events. This work evaluates its performance characteristics following the National Electrical Manufacturers Association (NEMA) NU4-2008 protocol. The S-PET consists of twenty flat panel type detectors arranged in two rings. The inner diameter is 80 mm and the axial field of view (FOV) is 104.5 mm. Each detector is comprised of two layers of phoswich scintillator crystal arrays, an oblique edge cut glass lightguide and two multi-

pixel photon counter (MPPC) arrays. The front (annihilation photon entrance) layer is a 30 × 60 pixelated cerium doped lutetium yttrium orthosilicate (LYSO) scintillator array with individual crystals measuring 0.79 × 0.79 × 5 mm^3. The back (towards the MPPCs) layer is a 20 × 40 pixelated bismuth germanate (BGO) scintillator array with individual crystals measuring 1.22 × 1.22 × 7.5 mm^3. For energy windows 350–650 keV, the peak absolute sensitivity at the center of the FOV was 14.9% including CLCS events, and 11.9% excluding CLCS events. The average system energy resolution derived by averaging the individual crystal spectra was 11.2% ± 3.1% for LYSO and 28.3% ± 5.8% for BGO. The 3D ordered-subsets expectation maximization (OSEM) reconstructed image with spatially variant point spread function (PSF) modeling of a point source in air, ranged from 0.65 mm to 1.08 mm, with an average value of 0.78 ± 0.12 mm at all measured locations. The peak noise equivalent count rate (NECR) and scatter fractions were 237.4 kcps at 11.9 MBq and 13.0% for the mouse-sized phantom, and 110.3 kcps at 11.9 MBq and 23.3% for the rat-sized phantom. For the NEMA image quality phantom, the uniformity was 6.3%, and the spillover ratios measured in the water- and air-filled cold region chambers were 11.1% and 7.9%, respectively. The recovery coefficients (RC) ranged from 0.36 to 0.89. The comprehensive results demonstrate that S-PET developed at SZBL possesses high spatial resolution and high sensitivity, which meets the requirements of preclinical research, such as mouse and rat imaging.

Keywords: small animal imaging, PET, performance evaluation, instrumentation, molecular imaging, depth-of-interaction

Submitted to: *Phys. Med. Biol.*

1. Introduction

Positron emission tomography (PET) is a non-invasive functional imaging modality widely employed in nuclear medicine, leveraging the detection of coincidence back-to-back gamma rays produced by positron annihilation. Since pathological functional alterations often precede structural changes, PET plays an essential role in the early diagnosis and longitudinal monitoring of malignancies, cardiovascular conditions, and neurological disorders[1]. In particular, preclinical PET systems optimized for imaging small animal models, have become indispensable in biomedical research, facilitating advances in disease modeling, drug development, and therapy assessment[2].

However, imaging small subjects such as mice, which possess approximately 1/3000 the volume of humans and exhibit considerably faster metabolic rates, imposes significantly stricter requirements on spatial resolution and system sensitivity compared to clinical PET systems[3, 4, 5, 6]. A fundamental challenge in achieving high and uniform spatial resolution lies in mitigating parallax error, which arises when annihilation photons enter detectors at oblique angles causing event mispositioning. This degradation becomes progressively more severe from the center to the edge of the field-of-view (FOV), making accurate depth-of-interaction (DOI) encoding essential for reliable quantification in small animal studies.

These demanding requirements have driven substantial innovations in detector technology, with research efforts focusing on achieving simultaneously high spatial resolution and system sensitivity. Among the key strategies, reducing the cross-section of the crystal represents a fundamental approach for improving spatial resolution, enabling the visualization of small structures in rodent organs that are essential for preclinical research[7, 8, 9]. In addition, the employment of high-Z scintillator materials significantly enhances system sensitivity by improving gamma-ray stopping power, which is particularly important for detecting the weak signals from low radiotracer doses administered to small animals. This approach facilitates the use of thinner scintillators and improves the signal-to-noise ratio, thereby allowing for more accurate quantification of radiotracer uptake in small regions of interest (ROI)[10, 11, 12]. Phoswich detector designs that incorporate multiple scintillator layers effectively address parallax errors by enabling accurate DOI measurement while maintaining system sensitivity through scintillator crystals with enough thickness[13, 14]. This combined improvement in both spatial resolution and detection efficiency ensures uniform performance across the entire FOV.

Among existing preclinical systems[15, 16, 17, 18], the HiPET system [19] developed at University of California Los Angeles represent a notable advancement, incorporating dual-layer phoswich detectors with lutetium yttrium orthosilicate (LYSO) and bismuth germanate (BGO) crystals to achieve excellent spatial resolution and high sensitivity. Despite these advancements, opportunities remain for improving spatial resolution, compactness, and photon detection efficiency.

In this work, we present S-PET, a next-generation, benchtop small animal PET

prototype developed at Shenzhen Bay Laboratory (SZBL) as an upgrade to the HiPET system. Building upon HiPET's phoswich detector architecture, S-PET incorporates silicon photomultiplier (SiPM) for scintillation light readout, replacing traditional photomultiplier tubes (PMTs), significantly enhancing the compactness and scalability of the system. Furthermore, the system employs smaller scintillator crystals and a reduced ring diameter to improve spatial resolution and sensitivity.

To thoroughly evaluate these enhancements, a comprehensive performance assessment of the S-PET system was conducted following the National Electrical Manufacturers Association (NEMA) NU 4-2008 standards [20], including sensitivity, spatial resolution, scatter fraction (SF), count-rate performance and image quality with necessary adaptions. Additionally, *in vivo* rodent studies using radiolabeled tracers were conducted to demonstrate the capability of this system for high sensitivity, high resolution preclinical research. Representative animal images are shown to highlight the molecular information provided by this prototype.

2. Materials and methods

2.1. System description

A photograph of the prototype S-PET scanner is shown in figure 1(a). The S-PET system consists of twenty flat panel detectors arranged in two rings. The detector ring inner diameter is 80 mm and the axial FOV is 104.5 mm. Each detector is comprised of two layers of pixelated scintillator arrays (Ningbo EBO Optoelectronics, Ningbo, China), a glass light guide with oblique edge cuts and two 8 × 8 multi-pixel photon counter (MPPC) arrays, as shown in figure 1(b). The front (annihilation photon entrance) scintillator layer is a 30 × 60 array of 0.79 × 0.79 × 5 mm^3 LYSO crystals (0.87 mm pitch). The back layer (towards the MPPCs) is a 20 × 40 array of 1.22 × 1.22 × 7.5 mm^3 BGO crystals (1.30 mm pitch). LYSO and BGO scintillator elements are multiplexed in a ratio of 9:4, with each 3 × 3 LYSO array segment coupled to a 2 × 2 BGO array segment. The LYSO and BGO crystal elements were mechanically polished on all sides except for the ends towards the lightguide, which were diffusely ground. Each individual crystal was bonded with an Enhanced Specular Reflector (ESR) (3M, St Paul, MN, USA). A glass light guide with oblique edge cuts (from top to bottom, cut from 1.81 mm to 2.61 mm from the edge and filled with ESR, figure 1(c)) was used to couple the exit end of the BGO crystal array (26 × 52 mm^2) to the photosensitive area containing two S14161-3050HS-08 low breakdown voltage type MPPCs (Hamamatsu Photonics, Hamamatsu City, Japan). The detector module has overall dimensions of 26 mm in the transaxial direction and 52 mm in the axial direction. This matches the total external dimensions of two MPPCs, allowing continuous positioning of the scintillator arrays and seamless assembly axially. (see figure 1(b)). The scintillator array, lightguide and two MPPCs were bonded with optical grease. All pixels of the two 64-channel MPPCs were read out by a 128-channel front-end module (FEM128) comprising two TOFPET2

application-specific integrated circuits (ASICs) (PETsys Electronics, Oeiras, Portugal).

Data from all 20 detector modules were delivered to 3 FEB/D_v2 boards, which also provided power for the ASICs and MPPCs. System clock and a coarse coincidence filter were provided by a Clock&trigger module. A DAQ board was used to receive data from the FEB/D_v2 and transmit the data to the computer. Given that the ASICs are close to the MPPCs and are a source of heat, customized aluminum pipes were coupled to the ASICs via thermal grease. Water cooled by a Peltier module flows continuously through the pipes. The temperature of the MPPCs was kept at about 26°C with a < 1°C variation. Before data acquisition, all ASICs were calibrated following a routine provided by PETsys. More details on data processing can be found in [21].

The acquired data were post-processed using a two-dimensional look-up-table (see figure 2) to distinguish three kinds of events (LYSO, BGO and CLCS, cross layer crystal scatter)[21]. The signal of the LYSO will be the main component of the CLCS events since the light output of LYSO is much greater than that of BGO. Therefore, the LYSO post-processing parameters, such as timing peaks and crystal look-up-tables, were used when processing CLCS events. No energy windows were applied for CLCS events.

The characteristics of the S-PET systems are summarized in table 1.

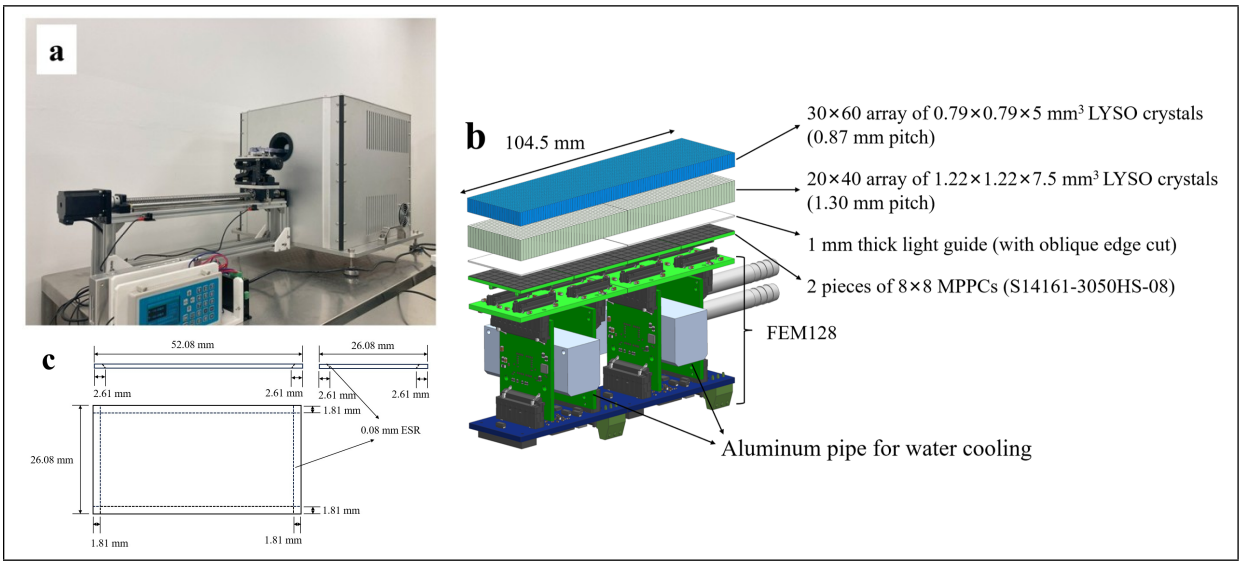

Figure 1. (a) Photograph of the S-PET system; (b) schematic of two detector modules arranged axially; (c) schematic of the oblique edge cut light guide.

2.2. Energy and time resolution

A cylindrical phantom with diameter of 40 mm and 120 mm length was filled with 4.44 MBq (120 μCi) ^{18}F solution and placed at the center of the field of view (CFOV). Energy spectra of individual crystals were extracted, and a Gaussian function was fitted to the photopeak of each energy spectrum. The energy resolution was measured for every crystal in the scanner as the full width at half-maximum (FWHM) of the Gaussian

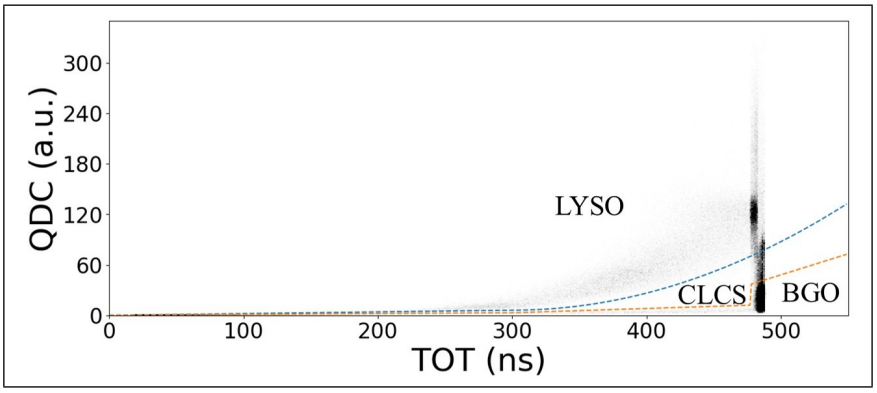

Figure 2. A two-dimensional charge integration (QDC) and time over threshold (TOT) histogram and a three region look-up-table to distinguish LYSO, BGO and CLCS events.

Table 1. Characteristics of the S-PET system, units of mm.

Crystal material	LYSO/BGO
Crystal size (mm^3)	$0.79 \times 0.79 \times 5/1.22 \times 1.22 \times 7.5$
Crystal pitch (mm)	0.87/1.30
Crystal array	$30 \times 60/20 \times 40$ crystals/2 MPPCs
Light guide	Oblique edge cut light guide (1.81–2.61 mm)
MPPC	Hamamatsu S14161-3050HS-08 MPPC
Number of rings	2
Number of detectors per rings	10
Number of crystals per module	2600
Number of crystals in total	52 000
Ring diameter (mm)	80
Axial FOV (mm)	104.5
Transaxial FOV (mm)	60
Signal processing system	TOFPET2 ASIC
Number of lines of responses (LORs)	6.76×10^8
Data format	List-mode

function divided by the energy corresponding to the center of the photopeak, expressed as a percentage resolution. Timing spectra between different detector pairs and event types were extracted and a Gaussian function was fitted to the peak of each timing spectrum. Coincidence timing resolution (CTR) was measured as the FWHM of the Gaussian function.

2.3. Spatial resolution

A 0.44 MBq ^{22}Na point source with diameter of 0.25 mm, embedded in a 1 cm^3 piece of acrylic was used (NEMA NU-4 compliant, Eckert & Ziegler Isotope Products, Valencia, CA, USA). The point source was imaged at two axial locations: (a) the center of the axial FOV and (b) one fourth of the axial FOV, at 26.1 mm from the center along the axial direction. For each of these two axial locations, the source

was placed radially offset at 0 mm, 5 mm, 10 mm, 15 mm and 25 mm from the geometric axis. Acquisition time was 30 s at each position and more than 10^5 prompt counts were acquired per measurement. Following the NEMA protocol, images were reconstructed using the filtered backprojection (STIR[22], FBP 2D) method with the CLCS events excluded. In addition, images were reconstructed using the 3D ordered-subsets expectation maximization (OSEM) algorithm (CASToR[23]) with image based spatially variant point spread function (PSF) modeling. The spatially variant PSFs were obtained by fitting the point source simulation data using double Gaussian functions at different positions[24]. The data was reconstructed using 3D OSEM with 3 iterations and 10 subsets, at an image voxel size of $0.2 \times 0.2 \times 0.2$ mm^3. The point source response function was formed by summing 1D profiles parallel to the radial, tangential, and axial directions of the reconstructed image. A parabolic fit of the peak point and its two nearest neighboring points was used to determine the maximum value of the response function. Linear interpolation between adjacent pixels was used to determine the position of the half and one tenth of the parabolic curve maximum. Measurements were not corrected for the physical source dimensions, positron range, or non-collinearity of positron annihilation gammas.

2.4. Sensitivity

The same ^{22}Na point source used for the spatial resolution measurement was also used to measure absolute system sensitivity. The activity of the point source was 0.44 MBq, low enough so that the counting loss due to deadtime was less than 1% and the random event rate was less than 5% of the true event rate, fulfilling the NEMA NU-4 recommendations. The axial sensitivity profile was measured with the ^{22}Na source stepped from end to end of the axial FOV. The number of coincidences was recorded at each position for 60 s. Background measurements (without any source) were collected in separate 60s acquisitions to account for contributions from the ^{176}Lu. Random and intrinsic events were subtracted from prompts before the true coincidences were divided by the actual source activity. The absolute sensitivity (percentage) was corrected for the branching ratio of ^{22}Na (0.906), see equation (1). The attenuation of the acrylic material surrounding the point source was not compensated,

$$S_A(\%) = \frac{100 \times (R_{prompt} - R_{random} - R_{intrinsic})}{A_{cal} \times 0.906}, \tag{1}$$

where $S_A(\%)$ is the absolute sensitivity (percentage), R_{prompt} and R_{random} are the prompt and random count rates respectively, $R_{intrinsic}$ is the intrinsic count rate of the scanner obtained from the background measurement and A_{cal} is the calibrated activity at the acquisition time.

The average sensitivities for a mouse-sized object (with a 70 mm axial length) and a rat-sized object (104.5 mm, corresponding to the system axial length) was calculated from the measured axial sensitivity profile.

2.5. Scatter and count-rate performance

The count-rate performance was evaluated using the NEMA NU-4 mouse- and rat-sized phantoms. The mouse-sized phantom is a solid cylinder measuring 70 mm in length and 25 mm in diameter, with a 3.2 mm diameter cylindrical hole drilled parallel to the central axis at a radial offset of 10 mm. The rat-sized phantom is a solid cylinder measuring 150 mm in length and 50 mm in diameter, with a 3.2 mm diameter cylindrical hole drilled parallel to the central axis at a radial offset of 17.5 mm. These solid cylinders are made of high density polyethylene (0.96 $\mathrm{g{\cdot}m^{-3}}$). A flexible tubing filled with ^{18}F solution was inserted into the 3.2 mm cylindrical hole of the phantom. The initial activity was measured to be 25 and 24 MBq for the mouse- and rat-sized phantom respectively using a dose calibrator (CRC-55tR, Capintec, Ramsey, NJ, USA) at the start of the acquisition. Background measurements were also collected in separate 20-minute acquisitions for both phantoms to account for contributions from the ^{176}Lu.

The data was post-processed with an energy window of 350–650 keV and timing windows of 2.4 ns, 6.4 ns and 9.6 ns for the LYSO-LYSO, LYSO-BGO and BGO-BGO coincidences, and with the CLCS events excluded. The SF was measured using a prompt sinogram with an activity of 111 kBq (3 μCi). This low-activity acquisition was chosen to ensure that dead time and randoms did not affect the measurement. As specified by NEMA NU-4, the scatter count rate was calculated by equation (2):

$$R_{scatter} = R_{prompt} - R_{true} - R_{random} - R_{intrinsic}, \tag{2}$$

where $R_{scatter}$, R_{prompt}, R_{true} and R_{random} are the scatter, prompt, true and random count rates respectively, and $R_{intrinsic}$ is the intrinsic count rate of the scanner obtained from the background measurement. The SF was calculated by equation (3):

$$\mathrm{SF} = \frac{R_{scatter}}{R_{scatter} + R_{true}}. \tag{3}$$

The noise equivalent count rate (NECR) was defined by equation (4):

$$\begin{aligned} \mathrm{NECR} &= \frac{R_{true}^2}{R_{prompt} + R_{random}} \\ &= \frac{(R_{prompt} - R_{random} - R_{intrinsic})^2 \times (1 - \mathrm{SF})^2}{R_{prompt} + R_{random}}. \end{aligned} \tag{4}$$

2.6. Imaging studies

For all imaging studies in this work, the data were post-processed with an energy window of 350–650 keV and a timing window of 2.4 ns, 6.4 ns and 9.6 ns for the LYSO-LYSO, LYSO-BGO and BGO-BGO coincidences, and with the CLCS events excluded.

2.6.1. NEMA image quality phantom Image quality studies were performed using the NEMA NU-4 image quality phantom (Data Spectrum, Durham, NC, US). The phantom was filled with 3.7 MBq of ^{18}F solution and data was acquired for 20 min

as prescribed in the NEMA NU-4 protocol. The data was reconstructed using 3D OSEM iterative reconstruction with a voxel size of $0.2 \times 0.2 \times 0.2$ mm^3. Detector efficiency normalization correction was applied, but no scatter correction was applied. A CT scan (the Madiclab Prime H Series, Madiclab, Linyi, China) of the phantom and its supporting bed was acquired and the reconstructed CT image defining the data acquisition geometry was forward projected through the PET system response matrix to generate attenuation correction for the PET data. OSEM iterations were set to 20 using 10 subsets with spatially variant PSF modeling and regularization (Nuyts[**?**], hyperparameter value 2). A 22.5 mm-diameter and 10 mm-high cylindrical ROI was drawn over the center of the uniform region of the image-quality phantom. The average concentration values and percentage standard deviation (% SD) in this ROI were used to estimate the uniformity performance as a measure of noise. The image slices covering the central 10 mm length of the rods were averaged to obtain a single 2D image slice of lower noise. Circular ROIs were drawn in this 2D image around each rod, with diameters twice the physical diameters of the rods. The maximum values in each of these ROIs were measured and divided by the mean value obtained in the uniformity test to obtain the recovery coefficient (RC) for each rod size. The transverse image pixel coordinates of the locations with the maximum ROI values were recorded and used to create 10 mm long line profiles along the rods in the axial direction. The SD of the pixel values measured along each of these line profiles was calculated. Although no object scatter correction was applied to the acquired dataset, the spillover ratio of the water- and air-filled cold region chamber were calculated as specified in the NEMA NU-4 standard to provide a rough estimation of the photon scatter effects. The diameter of the VOI was 4 mm and encompassed the central 7.5 mm in length in the axial direction. The ratio of the mean in each cold region to the mean of the hot uniform area was reported as spillover ratio.

2.6.2. Hot rod phantom Spatial resolution was also assessed with a Derenzo style hot rod phantom (Phantech, Madison, WI, US) with fillable channels of different diameters (0.5, 0.6, 0.75, 1.0, 1.25, and 1.5 mm) and center-to-center spacing two times the diameter of the respective channels. The phantom was filled with 1.85 MBq (50 μCi) of ^{18}F at the start of the acquisition and scanned for 30 min. The data were reconstructed using 3D OSEM iterative reconstruction with a voxel size of $0.2 \times 0.2 \times 0.2$ mm^3. Detector efficiency normalization correction was applied, but no scatter and attenuation correction was applied. OSEM iterations were set to 60 using 10 subsets with spatially variant PSF modeling.

2.6.3. Animal studies Animal studies were approved by the SZBL Animal Research Committee and carried out according to the guidelines of the Department of Laboratory Animal Medicine at SZBL.

For mouse studies, C57BL6 mouse was consciously injected intravenously via tail vein with approximately 10.1 MBq (274 μCi) [^{18}F]FDG. The mouse was then transferred

to a dedicated imaging chamber for PET imaging under anesthesia. The PET scans was acquired for 30 min after 115 min from the injection. Then the entire imaging chamber with the mouse was manually transferred to the same CT system used in phantom studies for CT acquisition.

For rat studies, a Sprague Dawley (SD) rat was consciously injected intravenously via tail vein with approximately 8.7 MBq (236 μCi) [^{18}F]FDG. The rat was then transferred to a dedicated imaging chamber for PET imaging under anesthesia. The imaging chamber was moved into the PET system with the brain of the rat placed approximately at the CFOV. The PET scan was acquired for 30 min after 90 min from the injection. After the PET scan, the entire imaging chamber with the rat was manually transferred to the same CT system for CT acquisition.

All animal PET images were reconstructed with an energy window of 350–650 keV using spatially variant PSF 3D OSEM with a voxel size of 0.2 × 0.2 × 0.2 mm^3. Corrections for photon attenuation (based on CT) and detector efficiency normalization were applied during reconstructions. For mouse imaging, OSEM iterations were set were set to 10 using 10 subsets. And for rat imaging, OSEM iterations were set to 5 using 10 subsets.

3. Results

3.1. Energy and time resolution

For the crystals in all twenty detectors, the average energy resolution as derived by averaging the energy resolution of the individual crystal spectra, was 11.2% ± 3.1% for LYSO and 28.3% ± 5.8% for BGO. Representative crystal energy spectra are shown in figure 3(a) (LYSO) and (b) (BGO). The CTR was 0.76 ± 0.08 ns, 2.06 ± 0.25 and 3.17 ± 0.46 ns for LYSO-LYSO, LYSO-BGO and BGO-BGO coincidences, respectively. Representative timing spectra for different event types are shown in figure 3(c).

3.2. Spatial resolution

Figure 4 shows the reconstructed image spatial resolution in the radial, tangential, and axial directions measured in the transverse plane at the axial center and at 1/4 axial offset using the spatially variant PSF modeling 3D OSEM (3 iterations, 10 subsets). The spatial resolution ranges from 0.65 mm to 1.08 mm, with an average value of 0.78 ± 0.12 mm. The full width tenth maximum (FWTM) ranges from 1.38 mm to 2.10 mm, with an average value of 1.67 ± 0.20 mm. The volumetric resolution varies from 0.34 to 0.73 μl. The asymmetric and spatially variant PSF modeling and the DOI decoding can effectively enhance image resolution, improve resolution uniformity across the FOV, and correct misposition and distortion in the reconstructed images. Following the NEMA protocol, the image spatial resolution obtained from FBP 2D reconstruction is shown in figure 5 and figure 6. For the LYSO-LYSO coincidences, the spatial resolution ranges from 0.54 mm to 1.77 mm, with an average value of 0.94 ± 0.28 mm. The FWTM

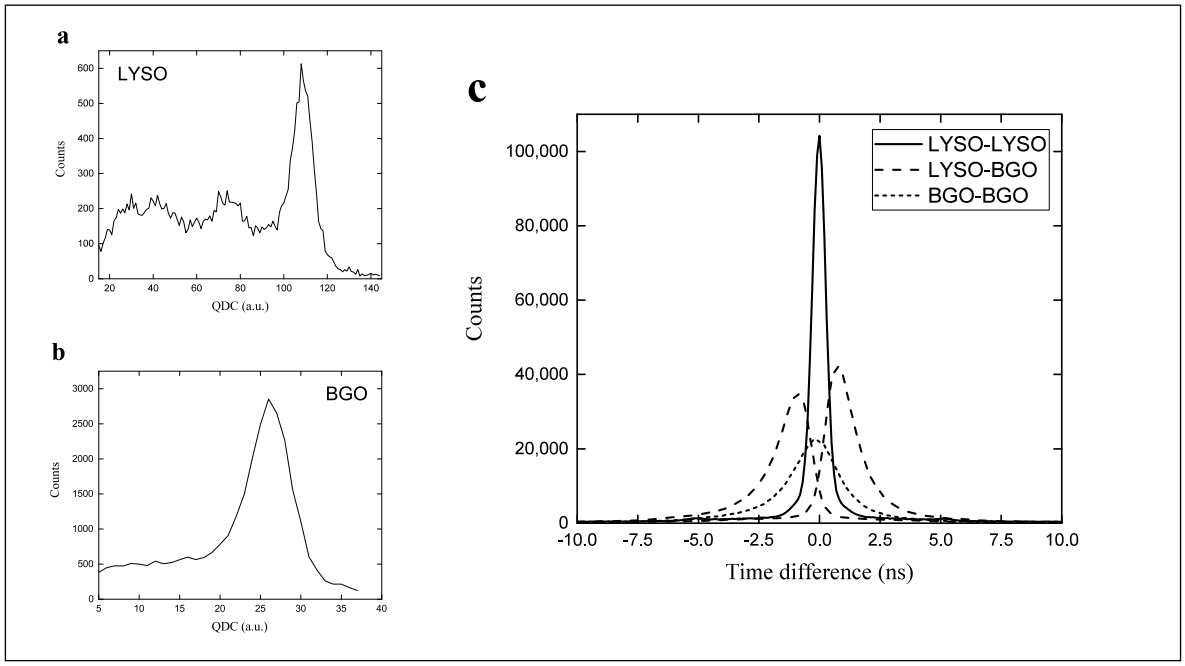

Figure 3. Representative crystal energy spectra of LYSO (a) and BGO (b) events, and representative timing spectra for different event types (c).

ranges from 1.26 mm to 3.13 mm, with an average value of 2.18 ± 0.41 mm. For the BGO-BGO coincidences, the spatial resolution ranges from 0.70 mm to 2.02 mm, with an average value of 1.33 ± 0.36 mm. The FWTM ranges from 1.27 mm to 4.10 mm, with an average value of 2.76 ± 0.67 mm.

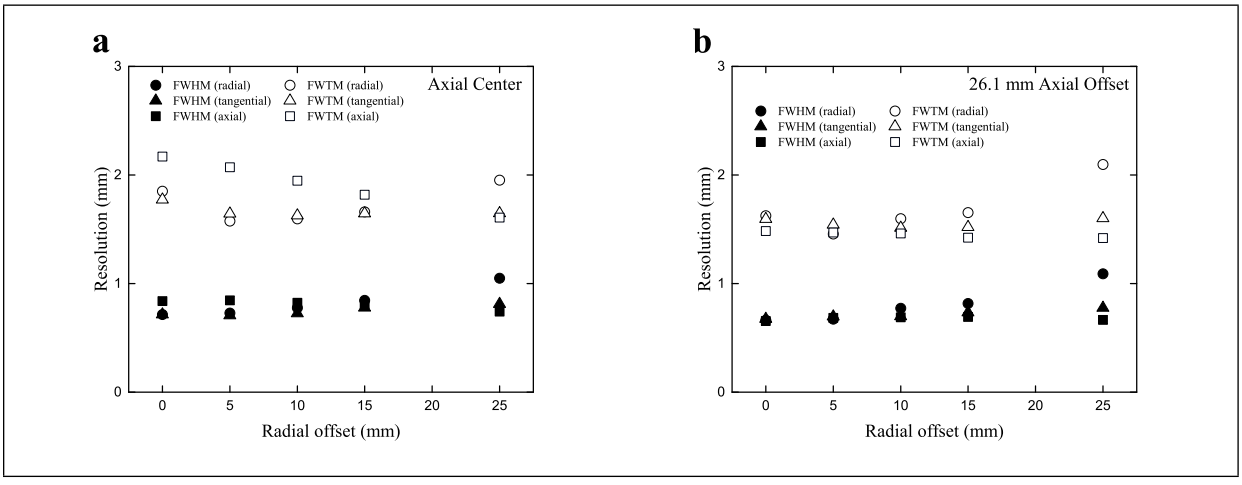

Figure 4. Reconstructed image spatial resolution (the spatially variant PSF modeling 3D OSEM, 3 iterations, 10 subsets) of the S-PET system, showing the FWHM and FWTM of the radial, tangential, and axial image resolution at (a) axial center of the FOV and (b) 26.1 mm from the axial center towards the axial edge of the FOV.

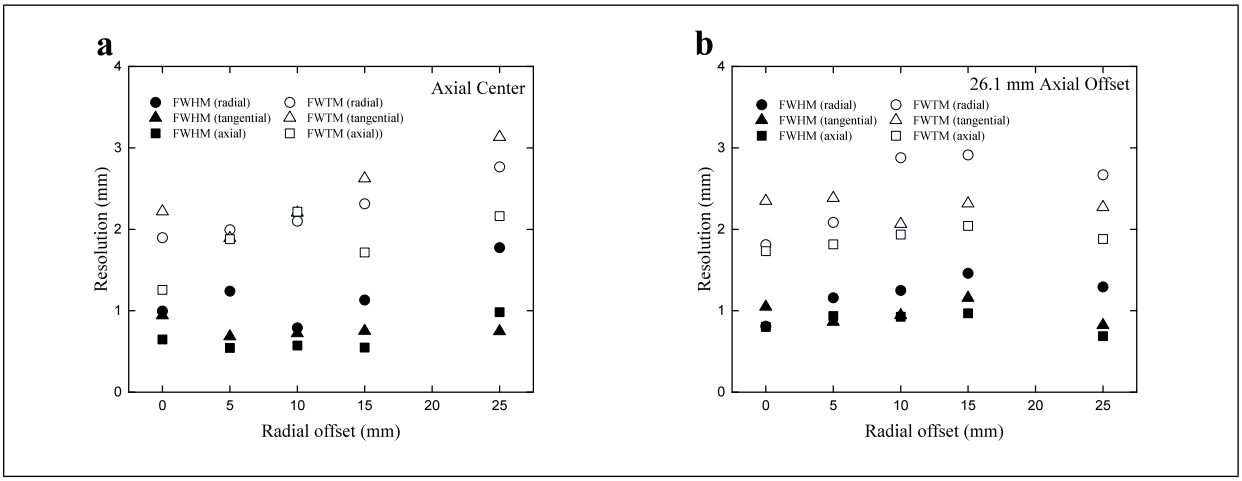

Figure 5. Reconstructed image spatial resolution (FBP 2D) of the S-PET system, showing the FWHM and FWTM of the radial, tangential, and axial image resolution for the LYSO-LYSO coincidences at (a) axial center of the FOV and (b) 26.1 mm from the axial center towards the axial edge of the FOV.

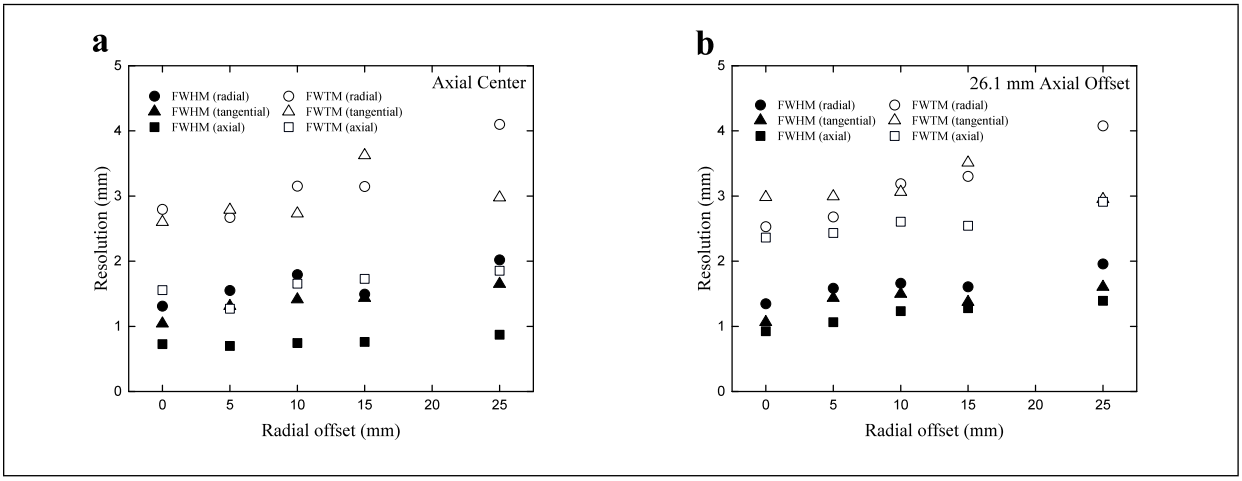

Figure 6. Reconstructed image spatial resolution (FBP 2D) of the S-PET system, showing the FWHM and FWTM of the radial, tangential, and axial image resolution for the BGO-BGO coincidences at (a) axial center of the FOV and (b) 26.1 mm from the axial center towards the axial edge of the FOV.

3.3. Sensitivity

Table 2 shows the absolute system sensitivity for different energy window settings at the CFOV ($S_{A,CFOV}$) and for the mouse and rat representative lengths ($SM_{A,tot}$ and $SR_{A,tot}$). The peak point source absolute system sensitivity is 14.9% (including the CLCS events) 11.9% (excluding the CLCS events) measured at the CFOV with a lower level discriminator (LLD) of 350 keV and an upper level discriminator (ULD) of 650 keV. The average sensitivity for a mouse-sized object (70 mm axial length) $SM_{A,tot}$ ranges from 11.5% to 22.6% (including the CLCS events) and 9.0% to 19.2% (excluding the CLCS events). The average sensitivity for a rat-sized object (104.5 mm system axial

Table 2. Absolute system sensitivity (%) as a function of LLD (with ULD = 650 keV) at the axial center of the FOV, for the mouse and rat representative lengths, and including or excluding the CLCS events.

	LLD (keV)	150	200	250	300	350
Without CLCS	$S_{A,\mathrm{CFOV}}$ (%)	24.2	21.3	18.1	15.0	11.9
	$SM_{A,tot}$ (%)	19.2	16.7	14.1	11.6	9.0
	$SR_{A,tot}$ (%)	16.1	13.9	11.6	9.4	7.3
With CLCS	$S_{A,\mathrm{CFOV}}$ (%)	28.4	25.3	21.9	18.4	14.9
	$SM_{A,tot}$ (%)	22.6	20.0	17.1	14.3	11.5
	$SR_{A,tot}$ (%)	19.0	16.6	14.1	11.7	9.3

length) $SR_{A,tot}$ ranges from 9.3% to 19.0% (including the CLCS events) and 7.3% to 16.1% (excluding the CLCS events). The axial sensitivity profiles for different energy window settings are shown in figure 7(a) (including the CLCS events) and (b) (excluding the CLCS events).

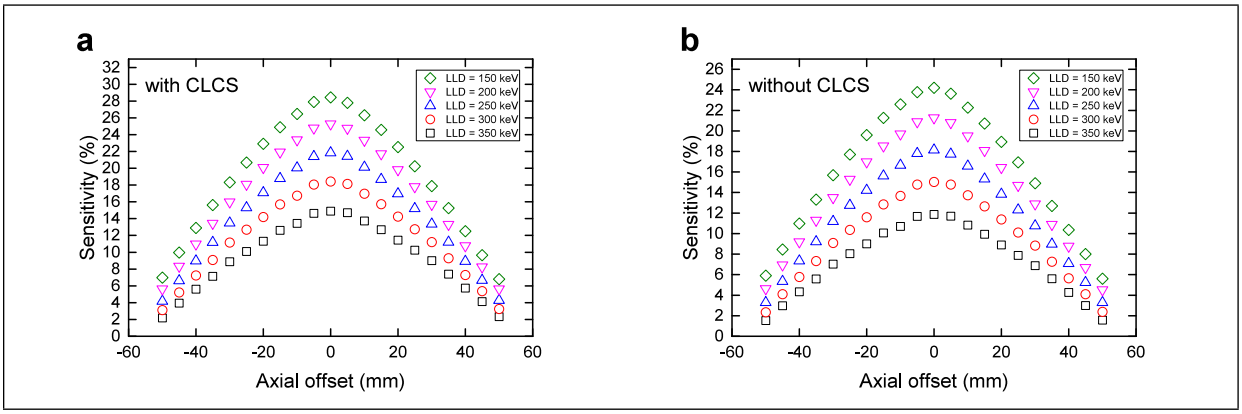

Figure 7. Absolute system sensitivity as function of axial position and with different energy windows (with ULD = 650 keV): (a) including the CLCS events; (b) excluding the CLCS events.

3.4. Scatter and count-rate performance

The prompt, random and NECR as a function of line source activity in the mouse- and rat-sized phantoms are plotted in figure 8(a) and (b). For the mouse-sized phantom, the peak NECR is 237.4 kcps at a total phantom activity of 11.9 MBq and the SF is 13.0%. For the rat-sized phantom, the peak NECR is 110.3 kcps at a total phantom activity of 11.9 MBq and the SF is 23.3%.

3.5. Imaging studies

3.5.1. NEMA image quality phantom Figure 9 shows images (0.2 mm thick slice) of a transverse plane of the uniform region (a), a transverse plane with the five resolution recovery rods (b), a coronal plane (c), and a profile across the uniform area (d)

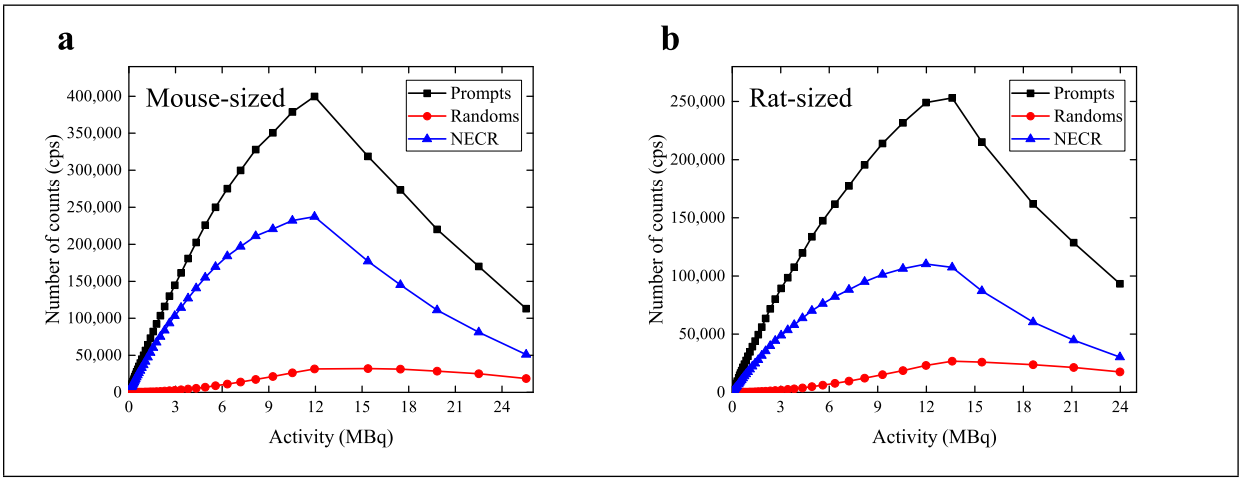

Figure 8. Count rate of the S-PET system as a function of line source activity: (a) mouse-sized phantom; (b) rat-sized phantom.

of the NEMA image quality phantom. With the variant PSF modeling 3D OSEM reconstruction (20 iterations, 10 subsets), the % SD in the uniform region was 6.3%. The RCs for the five different rod sizes from 1 to 5 mm diameter were 0.36 ± 0.06, 0.79 ± 0.07, 0.87 ± 0.08, 0.87 ± 0.07 and 0.89 ± 0.08. The SORs measured in the water and air filled cold region chambers were 11.1% ± 1.7% and 7.9% ± 1.4%.

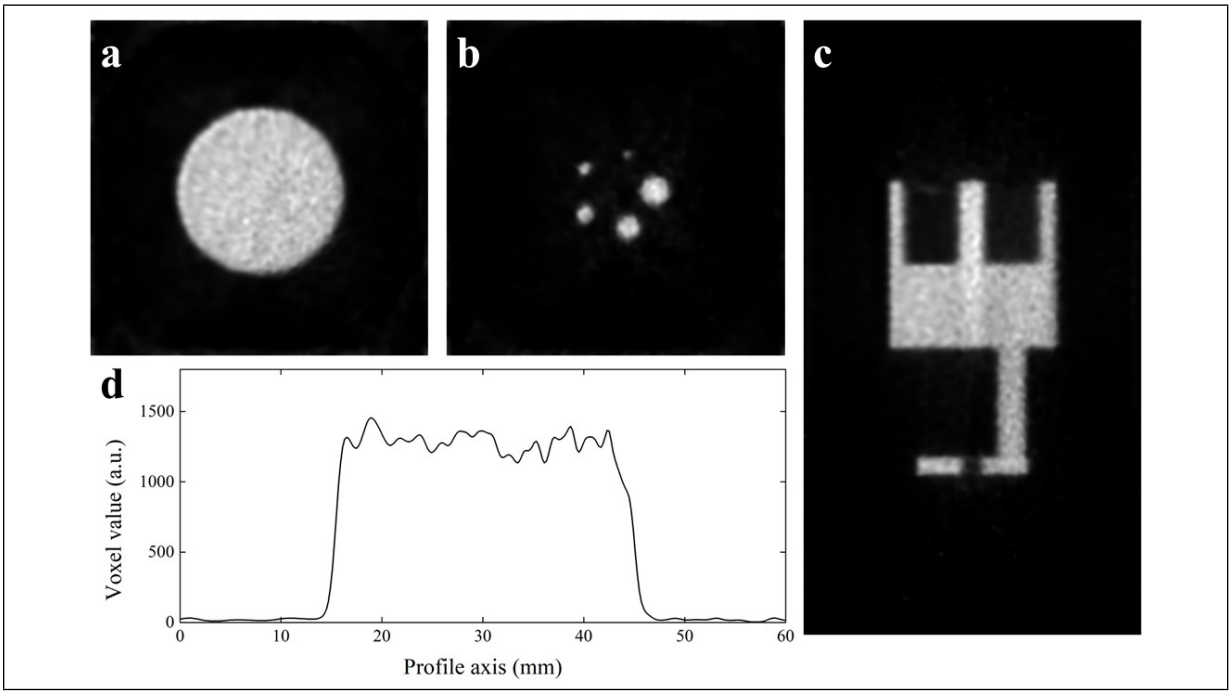

Figure 9. Reconstructed images of the NEMA NU-4 image quality phantom, filled with ^{18}F (3.7 MBq) and imaged for 20 min and reconstructed with the spatially variant PSF modeling 3D OSEM (20 iterations, 10 subsets): (a) a transverse slice of the uniform region; (b) a transverse slice of the rods region; (c) a coronal slice; (d) a profile across the uniform area.

3.5.2. Hot rod phantom Figure 10 shows the sum of transverse slices (6 mm thickness) in the rod area of the reconstructed image of the Derenzo style hot rod phantom (1.85 MBq ^{18}F, 30 min) with the spatially variant PSF modeling 3D OSEM (20 iterations, 10 subsets). The total number of prompt counts was 280 M. Although the positron range and photon non-collinearity are not corrected, all the rods with 0.75 mm diameter are resolvable in the reconstructed image.

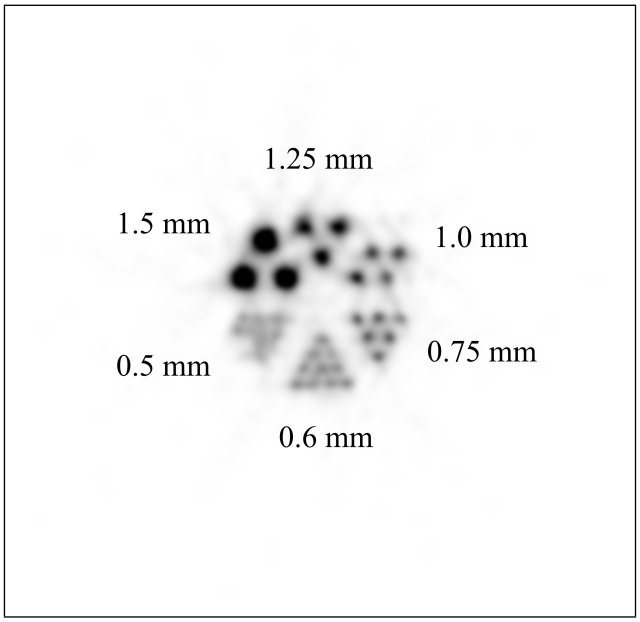

Figure 10. The sum of transverse slices (6 mm thickness) in the rod area of the reconstructed image of the Derenzo style hot rod phantom (0.5, 0.6, 0.75, 1.0, 1.25, 1.5 mm) imaged for 30 min and reconstructed with the spatially variant PSF modeling 3D OSEM (60 iterations, 10 subsets).

3.5.3. Animals study Representative images of the biodistribution of [^{18}F]FDG in a healthy mouse are shown in figure 11. Images show transverse, coronal and sagittal images from a 30 min [^{18}F]FDG study in a C57BL6 mouse, distinguishing the myocardium from blood pool and identifying other tissues such as kidney, intestine and bladder. The activity in the entire subject was approximately 4.92 MBq (133 μCi) at scan time.

Representative images of the biodistribution of [^{18}F]FDG in the head area of a healthy rat shown in figure 12. Images show transverse and coronal images from a 30 min [^{18}F]FDG study in a SD rat, distinguishing the difference uptake between the left and right region of the rat brain and identifying the cerebellum. The activity in the entire subject was approximately 5.00 MBq (135 μCi, about 1/10 of a normal rat PET scan) at scan time.

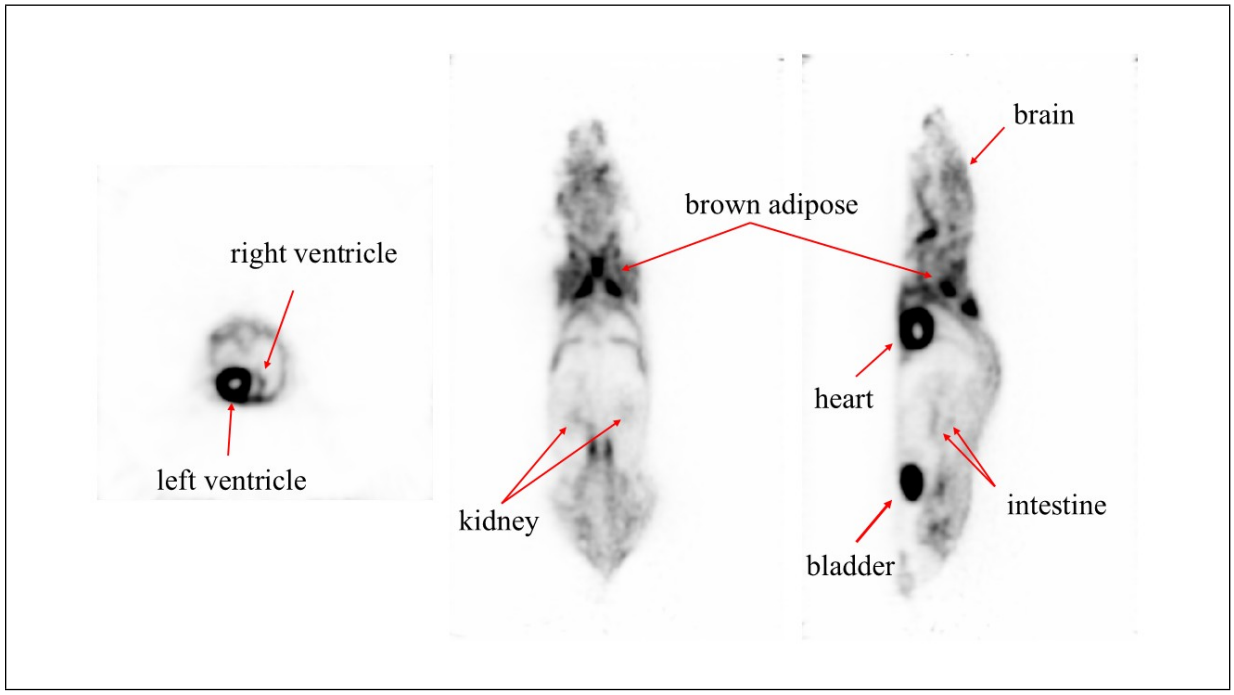

Figure 11. Representative images of 30 min static S-PET scan of a C57BL6 mouse imaged 105 min after injection with 10.1 MBq of [^{18}F]FDG (4.92 MBq at scan time).

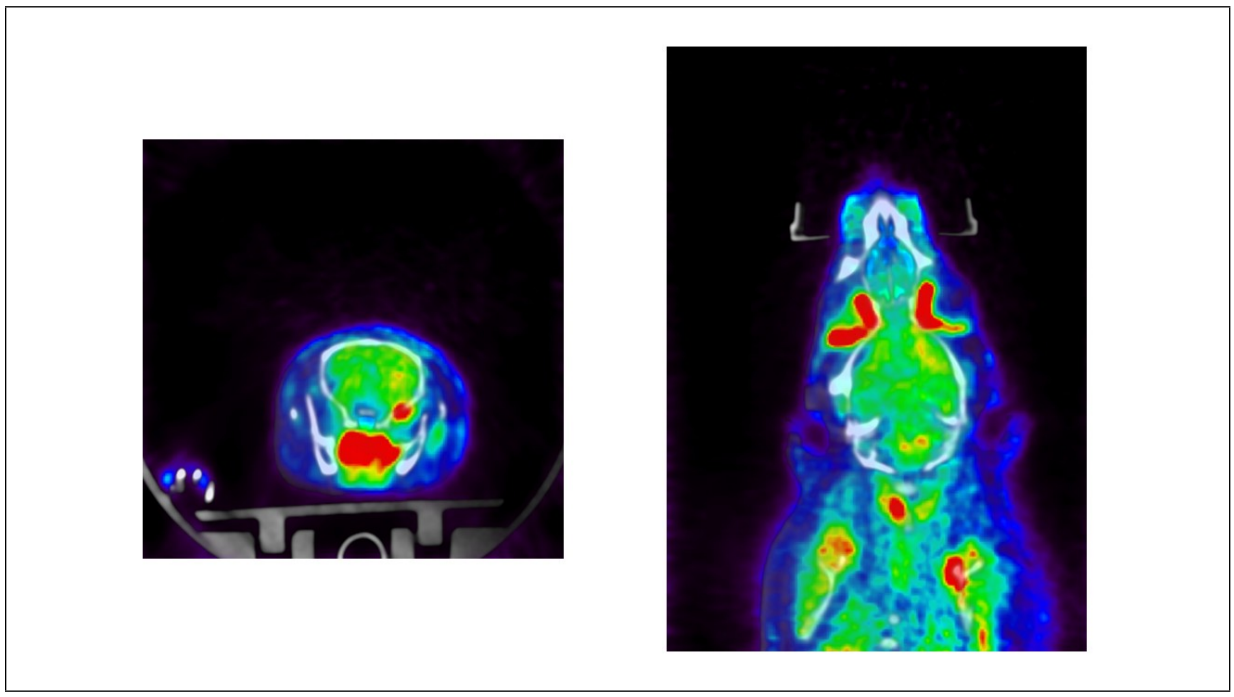

Figure 12. A fused PET-CT brain imaging of 30 min static S-PET scan of a SD rat imaged 90 min after injection with 8.7 MBq of [^{18}F]FDG (5.00 MBq at scan time).

4. Discussion and Conclusion

In this work, we evaluated the performance of the S-PET system, a next-generation preclinical PET prototype featuring a dual-layer LYSO/BGO phoswich detector, using the NEMA NU 4-2008 standards (with adaptations where necessary) alongside phantom and in vivo rodent studies. The DOI decoding methods utilizing different signal characteristics of stacked crystals have been widely applied [25, 26, 27, 28]. The system leverages the distinct signal characteristics of stacked LYSO/BGO crystals (30,000 vs. 8,000 photons/MeV; 40 ns vs. 300 ns decay time) to enable two-layers DOI resolution and CLCS events identification via a 2D lookup table [21]. The average LYSO system energy resolution was 11.2%, comparable to the HiPET system (11.7%)[19] and other preclinical PET systems, such as β-CUBE (12%)[29], Xtrim-PET (12.4%)[30], a long-axis animal PET (12.9%)[31] and a benchtop small-animal PET/MRI scanner (11.1% and 11.5%) [32]. However the average BGO system energy resolution was 28.3%, inferior to the HiPET (17.0%) and other BGO-only PET systems, such as the PETBox(19.6)%[10], the PETBox4 (18.0%)[33] and the G8 (19.3%)[34]. This degradation may be caused by truncated charge integration of the BGO signal, since the maximum charge integration time was set to 470 ns to balance the noise level of the signal and could not completely captures the slow decay BGO signal[21].

The S-PET system demonstrated CTR of 0.76 ns (LYSO-LYSO), 2.06 ns (LYSO-BGO), and 3.17 ns (BGO-BGO), representing significant improvement over the HiPET system (2.2, 4.8, and 6.6 ns respectively) due to its single-channel readout design. Event timing was determined using the earliest channel signal from two MPPCs after channel offset correction. The degraded BGO timing performance compared to LYSO results from its lower light output and slower decay time. These measurements, obtained with a cylindrical source to evaluate all possible LORs, showed slightly worse than our previous point source measurements (0.60, 1.50, and 2.52 ns)[**?**] due to light path variations in the extended source distribution. Since only the earliest timestamp was used for timing pickoff, the advantage of the single-channel readout was not fully realized. Several studies[35, 36, 37] showed the utilization of the neighbor channel signals could further improve the CTR. The fine timing resolution would reduce the random event rate and improve the quality of the coincidence events. For preclinical PET imaging, where the imaged object is small, a timing resolution of 200 ps (30 mm position uncertainty) would not help the image quality much with time-of-flight-based reconstruction[38]. Therefore, we think the timing resolution is acceptable at the current stage.

The spatial resolution of a PET system is limited by two physical factors, the crystal cross-section width and the non-collinearity of positron annihilation photons (determined by system diameter)[39]. Recent advances in high-resolution PET scanner development have employed increasingly smaller crystals, as demonstrated by several systems, Metis^{TM} (0.94 mm)[40], Hyperion II^{D} (0.93 mm)[41], submillimeter-resolution PET (0.9 mm)[42], an ultrahigh resolution Si-PM based PET system (0.5 mm, 0.32 mm)[43, 44], PawPET (0.43 mm)[45] and a prototype small-animal PET scanner (0.43

mm)[46]. The S-PET system improves upon HiPET's resolution (0.78 mm vs. 0.93 mm) through both smaller crystals (0.79 mm vs. 1.01 mm) and reduced detector ring diameter (80 mm vs. 160 mm). Reconstruction algorithms significantly impact resolution measurements, where OSEM with accurate system modeling provides more uniform resolution across the FOV and eliminates star artifacts characteristic of FBP[47, 48]. These artifacts, visible in figure 5(a) as the sudden rise of the radial FWHM at an offset of 5 mm and in figure 6(a) as crossed radial FWHM and axial FWTM curves, can distort resolution assessment. The system's imaging capability is further validated by the OSEM reconstructed hot rod phantom, which clearly resolves 0.75 mm diameter rods, demonstrating performance relevant to realistic small animal imaging conditions.

The sensitivity of a PET system is primarily determined by two factors, solid angle coverage (geometric efficiency) and crystal stopping power. Compared to the HiPET system with similar LYSO/BGO detector design and axial length (104.5 mm vs. 104 mm), the S-PET achieves superior performance through optimized geometry. Its smaller ring diameter (80 mm vs. 160 mm) increases solid angle coverage, helping improve the detection efficiency while reducing crystal thickness (12.5 mm vs. 15 mm). This design yields a 14.9% peak absolute sensitivity, outperforming HiPET (10.4%) and matching the SIAT aPET system (20 mm crystal thickness, 16.0%) [49] despite using less crystal material. The sensitivity also significantly exceeds the NanoPET/CT (13 mm crystal thickness, 7.7 %)[50] with comparable crystal thickness, due to the increased solid angle coverage and the usage of the high stopping power material, BGO. Such high sensitivity is particularly valuable for dynamic imaging studies, quantitative accuracy, and radiation dose reduction[51]. While dual-ended readout detectors[52] and four-layer designs [53, 54, 55] have been explored to improve sensitivity while mitigating the parallax errors, future S-PET upgrades will incorporate a four-layer LYSO/BGO phoswich detector (24 mm total thickness)[35] to further enhance sensitivity while preserving DOI accuracy and system geometry.

The S-PET system achieved a peak NECR of 237.4 kcps at 11.9 MBq for a mouse-sized phantom, representing a significant improvement over the HiPET system (179 kcps at 12.4 MBq) but occurring at lower activity levels compared to other preclinical scanners, such as β-CUBE (33.3 MBq)[29], Albira Si PET (22.58 MBq)[56] and SIAT aPET (26 MBq)[49]. In order to collect BGO signals, we have to set a very low threshold, thus including many low energy LYSO Compton events. This count rate limitation primarily caused by two reasons. The first is the substantial data generated by the single-channel readout, which uses a relatively low threshold. This threshold was set to collect weak BGO signals, but it also admits a large number of low-energy LYSO events, thereby pushing the data rate toward the physical bandwidth limits of the hardware. And the suboptimal data processing software increases system dead time and pileup events. Despite these limitations, the enhanced sensitivity of S-PET provides superior performance for typical preclinical studies using 10 MBq injected activities. Future implementations of multiplexed readout electronics[57] are expected to substantially reduce the amount of data and processing complexity, thereby reducing deadtime in the

electronics and improving overall count rate performance.

This study presents a comprehensive performance evaluation of the S-PET system, a next-generation small animal PET prototype featuring dual-layer LYSO/BGO phoswich detectors, developed at SZBL. Following NEMA NU 4-2008 standards with necessary adaptations, the results demonstrate significant improvements over the HiPET system with similar phoswich detector architecture. Achieveing a 0.78 mm image spatial resolution and a 14.9% peak sensitivity including the CLCS events, the S-PET could produce phantom and rodent images of high quality and would be a competitive platform for high resolution molecular imaging in preclinical research.

Acknowledgments

The authors would like to thank Drs. Arion F. Chatziioannou and David L. Prout of University of California, Los Angeles, for beneficial discussions. The authors also like to thank the staffs of the Cancer Hospital Chinese Academy of Medical Sciences for providing ^{18}F-ion and [^{18}F]-FDG. Some computations were carried out at the Shenzhen Bay Laboratory Supercomputing Center. This work is supported by the National Natural Science Foundation of China (No.12275182, No.12205204, No.62371314), Guangdong Basic and Applied Basic Research Foundation (No.2023A1515011293 and No.2024A1515012154), the National Key R&D Program of China (No.2023YFC2414800), the Major Program of Shenzhen Bay Laboratory (No. C1012530005) and the Shenzhen Bay Laboratory Proof-of-Concept Grants (No. C1022430005).

References

[1] Todd M. Blodgett, Carolyn C. Meltzer, and David W. Townsend. PET/CT: Form and function. *Radiology*, 242:360–385, 2 2007.

[2] Simon R. Cherry. In vivo molecular and genomic imaging: New challenges for imaging physics. *Physics in Medicine and Biology*, 49, 2 2004.

[3] Jennifer R. Stickel and Simon R. Cherry. High-resolution PET detector design: Modelling components of intrinsic spatial resolution. *Physics in Medicine and Biology*, 50:179–195, 1 2005.

[4] Robert S. Miyaoka and Adrienne L. Lehnert. Small animal PET: A review of what we have done and where we are going. *Physics in Medicine and Biology*, 65, 12 2020.

[5] Stephen S. Adler, Jurgen Seidel, and Peter L. Choyke. Advances in preclinical PET. *Seminars in Nuclear Medicine*, 52(3):382–402, 2022.

[6] Junwei Du and Terry Jones. Technical opportunities and challenges in developing total-body PET scanners for mice and rats. *EJNMMI Physics*, 10, 12 2023.

[7] R.S. Miyaoka, S.G. Kohlmyer, and T.K. Lewellen. Performance characteristics of micro crystal element (MiCE) detectors. *IEEE Transactions on Nuclear Science*, 48(4):1403–1407, 2001.

[8] Jennifer R. Stickel, Jinyi Qi, and Simon R. Cherry. Fabrication and characterization of a 0.5-mm lutetium oxyorthosilicate detector array for high-resolution pet applications. *Journal of Nuclear Medicine*, 48(1):115–121, 2007.

[9] Xi Zhang, Xin Yu, Heng Zhang, Changlin Liu, Hamid Sabet, Siwei Xie, Jianfeng Xu, and Qiyu Peng. Development and evaluation of 0.35-mm-pitch PET detectors with different reflector

arrangements. *IEEE Transactions on Radiation and Plasma Medical Sciences*, 7:802–809, 11 2023.

[10] Hui Zhang, Qinan Bao, Nam T. Vu, Robert W. Silverman, Richard Taschereau, Brittany N. Berry-Pusey, Ali Douraghy, Fernando R. Rannou, David B. Stout, and Arion F. Chatziioannou. Performance evaluation of PETbox: A low cost bench top preclinical PET scanner. *Molecular Imaging and Biology*, 13:949–961, 10 2011.

[11] Seiichi Yamamoto, Hiroshi Watabe, Yasukazu Kanai, Tadashi Watabe, Masao Imaizumi, Eku Shimosegawa, and Jun Hatazawa. Development of a high-sensitivity BGO well counter for small animal PET studies. *Radiological Physics and Technology*, 5:59–62, 1 2012.

[12] Junwei Du. Performance of dual-ended readout PET detectors based on BGO arrays and $BaSO_4$ reflector. *IEEE Transactions on Radiation and Plasma Medical Sciences*, 6:522–528, 5 2022.

[13] S. Yamamoto and H. Ishibashi. A GSO depth of interaction detector for pet. *IEEE Transactions on Nuclear Science*, 45(3):1078–1082, 1998.

[14] Tomoaki Tsuda, Hideo Murayama, Keishi Kitamura, Taiga Yamaya, Eiji Yoshida, Tomohide Omura, Hideyuki Kawai, Naoko Inadama, and Narimichi Orita. A four-layer depth of interaction detector block for small animal PET. *IEEE Transactions on Nuclear Science*, 51:2537–2542, 10 2004.

[15] Qinan Bao, Danny Newport, Mu Chen, David B. Stout, and Arion F. Chatziioannou. Perfrmance evalution of the inveon dedicated PET preclinical tomograph based on the NEMA NU-4 standards. *Journal of Nuclear Medicine*, 50:401–408, 3 2009.

[16] Fotini D. Popota, Pablo Aguiar, J. Raul Herance, Deborah Pareto, Santiago Rojas, Domenec Ros, Javier Pavia, and Juan Domingo Gispert. Comparison of the performance evaluation of the microPET r4 scanner according to nema standards nu 4-2008 and nu 2-2001. *IEEE Transactions on Nuclear Science*, 59:1879–1886, 2012.

[17] Andrew L. Goertzen, Qinan Bao, Melanie Bergeron, Eric Blankemeyer, Stephan Blinder, Mario Ca nadas, Arion F. Chatziioannou, Katherine Dinelle, Esmat Elhami, Hans Sonke Jans, Eduardo Lage, Roger Lecomte, Vesna Sossi, Suleman Surti, Yuan Chuan Tai, Juan Jose Vaquero, Esther Vicente, Darin A. Williams, and Richard Laforest. NEMA NU 4-2008 comparison of preclinical PET imaging systems. *Journal of Nuclear Medicine*, 53:1300–1309, 8 2012.

[18] Qingyang Wei, Shi Wang, Tianyu Ma, Jing Wu, Hui Liu, Tianpeng Xu, Yan Xia, Peng Fan, Zhenlei Lyu, and Yaqiang Liu. Performance evaluation of a compact PET/SPECT/CT tri-modality system for small animal imaging applications. *Nuclear Instruments and Methods in Physics Research, Section A: Accelerators, Spectrometers, Detectors and Associated Equipment*, 786:147–154, 6 2015.

[19] Zheng Gu, Richard Taschereau, Nam T. Vu, David L. Prout, Jason Lee, and Arion F. Chatziioannou. Performance evaluation of HiPET, a high sensitivity and high resolution preclinical PET tomograph. *Physics in Medicine and Biology*, 65, 2 2020.

[20] NEMA. NEMA Standards Publication NU 4-2008: Performance measurements of small animal positron emission tomographs, 2008.

[21] David L. Prout, Zheng Gu, Max Shustef, and Arion F. Chatziioannou. A digital phoswich detector using time-over-threshold for depth of interaction in PET. *Physics in Medicine and Biology*, 65, 12 2020.

[22] Kris Thielemans, Charalampos Tsoumpas, Sanida Mustafovic, Tobias Beisel, Pablo Aguiar, Nikolaos Dikaios, and Matthew W. Jacobson. STIR: Software for tomographic image reconstruction release 2. *Physics in Medicine and Biology*, 57:867–883, 2 2012.

[23] Thibaut Merlin, Simon Stute, Didier Benoit, Julien Bert, Thomas Carlier, Claude Comtat, Marina Filipovic, Frederic Lamare, and Dimitris Visvikis. CASToR: A generic data organization and processing code framework for multi-modal and multi-dimensional tomographic reconstruction. *Physics in Medicine and Biology*, 63, 9 2018.

[24] G. Li, X. Zhao, H. Yang, Y. Zhao, W. Huang, Y. Huang, M. Niu, Y. Liang, J. Wu, and Z. Gu. Resolution model with asymmetric and spatially-variant psfs for the s-PET system. In

2024 IEEE Nuclear Science Symposium (NSS), Medical Imaging Conference (MIC) and Room Temperature Semiconductor Detector Conference (RTSD), pages 1–2, 2024.

[25] J. Seidel, J.J. Vaquero, S. Siegel, W.R. Gandler, and M.V. Green. Depth identification accuracy of a three layer phoswich pet detector module. *IEEE Transactions on Nuclear Science*, 46(3):485–490, 1999.

[26] Jeffrey P. Schmall, Suleman Surti, and Joel S. Karp. Characterization of stacked-crystal PET detector designs for measurement of both tof and doi. *Physics in Medicine and Biology*, 60:3549–3565, 5 2015.

[27] Z. Gu, D. L. Prout, R. W. Silverman, H. Herman, A. Dooraghi, and A. F. Chatziioannou. A DOI detector with crystal scatter identification capability for high sensitivity and high spatial resolution PET imaging. *IEEE Transactions on Nuclear Science*, 62:740–747, 6 2015.

[28] Taek-Soo Lee, Andrew Rittenbach, Cesar Gutierrez Fernandez, Jesus Lopez-Longas, Juan M. Arco, and Benjamin M. W. Tsui. Initial evaluation of a state-of-the-art commercial preclinical PET/CT scanner. In *2016 IEEE Nuclear Science Symposium, Medical Imaging Conference and Room-Temperature Semiconductor Detector Workshop (NSS/MIC/RTSD)*, pages 1–4, 10 2016.

[29] Srilalan Krishnamoorthy, Eric Blankemeyer, Pieter Mollet, Suleman Surti, Roel Van Holen, and Joel S. Karp. Performance evaluation of the molecubes β-CUBE - a high spatial resolution and high sensitivity small animal PET scanner utilizing monolithic lyso scintillation detectors. *Physics in Medicine and Biology*, 63, 7 2018.

[30] Mahsa Amirrashedi, Saeed Sarkar, Pardis Ghafarian, Reza Hashemi Shahraki, Parham Geramifar, Habib Zaidi, and Mohammad Reza Ay. NEMA NU-4 2008 performance evaluation of Xtrim-PET: A prototype sipm-based preclinical scanner. *Medical Physics*, 46:4816–4825, 11 2019.

[31] Qing Wei, Yingjie Wang, Xianchao Huang, Daowu Li, Yushuang Zheng, Peilin Wang, Xiaoli Sun, Pei Chai, Xiaorou Han, Shuangquan Liu, Baotong Feng, Wei Zhou, Xiangtao Zeng, Meiling Zhu, Zhiming Zhang, and Long Wei. Performance evaluation of a small-animal PET scanner with 213 mm axis using NEMA NU 4-2008. *Medical Physics*, 2024.

[32] Xin Yu, Zhijun Zhao, Han Liu, Da Liang, Wenjing Zhu, Ying Lin, Jiayang Zeng, Chenxuan Liu, Jianfeng Xu, Siwei Xie, Weimin Wang, and Qiyu Peng. Development and performance evaluation of a benchtop small-animal PET/MRI scanner. *IEEE Transactions on Radiation and Plasma Medical Sciences*, 2025.

[33] Z. Gu, R. Taschereau, N. T. Vu, H. Wang, D. L. Prout, R. W. Silverman, B. Bai, D. B. Stout, M. E. Phelps, and A. F. Chatziioannou. NEMA NU-4 performance evaluation of PETbox4, a high sensitivity dedicated PET preclinical tomograph. *Physics in Medicine and Biology*, 58:3791–3814, 6 2013.

[34] Zheng Gu, Richard Taschereau, Nam T. Vu, David L. Prout, Robert W. Silverman, Jason T. Lee, and Arion F. Chatziioannou. Performance evaluation of g8, a high-sensitivity benchtop preclinical PET/CT tomograph. *Journal of Nuclear Medicine*, 60:142–149, 1 2019.

[35] Wen He, Yangyang Zhao, Xin Zhao, Wenjie Huang, Lei Zhang, David L. Prout, Arion F. Chatziioannou, Qiushi Ren, and Zheng Gu. A CNN-based four-layer DOI encoding detector using LYSO and BGO scintillators for small animal PET imaging. *Physics in Medicine and Biology*, 68, 5 2023.

[36] Xinjie Zeng, Zipai Wang, Wanbin Tan, Eric Petersen, Xinjie Cao, Andy LaBella, Anthony Boccia, Dinko Franceschi, Mony de Leon, Gloria Chia Yi Chiang, Jinyi Qi, Anat Biegon, Wei Zhao, and Amir H. Goldan. A conformal TOF-DOI Prism-PET prototype scanner for high-resolution quantitative neuroimaging. *Medical Physics*, 50:3401–3417, 6 2023.

[37] Eiji Yoshida, Fujino Obata, and Taiga Yamaya. Timing estimation of the exponentiated energy-weighted average for crosshair light sharing TOF-DOI PET detector. *Nuclear Instruments and Methods in Physics Research, Section A: Accelerators, Spectrometers, Detectors and Associated Equipment*, 1059, 2 2024.

[38] Nikta Zarif Yussefian, Maxime Toussaint, Emilie Gaudin, Roger Lecomte, and Rejean Fontaine. Tof benefits and trade-offs on image contrast-to-noise ratio performance for a small animal PET

scanner. *IEEE Transactions on Radiation and Plasma Medical Sciences*, 5:687–693, 9 2021.

[39] William W. Moses. Fundamental limits of spatial resolution in PET. *Nuclear Instruments and Methods in Physics Research, Section A: Accelerators, Spectrometers, Detectors and Associated Equipment*, 648, 8 2011.

[40] Qiong Liu, Chaofan Li, Jiguo Liu, Kishore Krish, Xinlei Fu, Jie Zhao, and Jyh Cheng Chen. Technical note: Performance evaluation of a small-animal PET/CT system based on NEMA NU 4-2008 standards. *Medical Physics*, 48:5272–5282, 9 2021.

[41] Patrick Hallen, David Schug, Bjoern Weissler, Pierre Gebhardt, Andre Salomon, Fabian Kiessling, and Volkmar Schulz. PET performance evaluation of the small-animal Hyperion IID PET/MRI insert based on the nema nu-4 standard. *Biomedical Physics and Engineering Express*, 4, 10 2018.

[42] Han Gyu Kang, Hideaki Tashima, Hidekatsu Wakizaka, Fumihiko Nishikido, Makoto Higuchi, Miwako Takahashi, and Taiga Yamaya. Submillimeter-Resolution PET for high-sensitivity mouse brain imaging. *Journal of Nuclear Medicine*, 64:978–985, 6 2023.

[43] Seiichi Yamamoto, Hiroshi Watabe, Yasukazu Kanai, Tadashi Watabe, Katsuhiko Kato, and Jun Hatazawa. Development of an ultrahigh resolution Si-PM based PET system for small animals. *Physics in Medicine and Biology*, 58:7875–7888, 11 2013.

[44] Seiichi Yamamoto, Hiroshi Watabe, Tadashi Watabe, Hayato Ikeda, Yasukazu Kanai, Yoshimune Ogata, Katsuhiko Kato, and Jun Hatazawa. Development of ultrahigh resolution Si-PM-based PET system using 0.32 mm pixel scintillators. *Nuclear Instruments and Methods in Physics Research, Section A: Accelerators, Spectrometers, Detectors and Associated Equipment*, 836:7–12, 11 2016.

[45] Felipe Godinez, Kuang Gong, Jian Zhou, Martin S. Judenhofer, Abhijit J. Chaudhari, and Ramsey D. Badawi. Development of an Ultra High Resolution PET Scanner for Imaging Rodent Paws: PawPET. *IEEE Transactions on Radiation and Plasma Medical Sciences*, 2:7–16, 1 2018.

[46] Yongfeng Yang, Julien Bec, Jian Zhou, Mengxi Zhang, Martin S. Judenhofer, Xiaowei Bai, Kun Di, Yibao Wu, Mercedes Rodriguez, Purushottam Dokhale, Kanai S. Shah, Richard Farrell, Jinyi Qi, and Simon R. Cherry. A prototype high-resolution small-animal PET scanner dedicated to mouse brain imaging. *Journal of Nuclear Medicine*, 57:1130–1135, 7 2016.

[47] A. Ram Yu, Jin Su Kim, Joo Hyun Kang, and Sang Moo Lim. Comparison of reconstruction methods and quantitative accuracy in Siemens Inveon PET scanner. *Journal of Instrumentation*, 10, 4 2015.

[48] Patrick Hallen, David Schug, and Volkmar Schulz. Comments on the NEMA NU 4-2008 standard on performance measurement of small animal positron emission tomographs. *EJNMMI Physics*, 7, 12 2020.

[49] Zhonghua Kuang, Xiaohui Wang, Ning Ren, San Wu, Juan Gao, Tianyi Zeng, Dongfang Gao, Chunhui Zhang, Ziru Sang, Zhanli Hu, Junwei Du, Dong Liang, Xin Liu, Hairong Zheng, and Yongfeng Yang. Design and performance of SIAT aPET: A uniform high-resolution small animal PET scanner using dual-ended readout detectors. *Physics in Medicine and Biology*, 65, 11 2020.

[50] Istvan Szanda, Jane Mackewn, Gergely Patay, Peter Major, Kavitha Sunassee, Gregory E. Mullen, Gabor Nemeth, York Haemisch, Philip J. Blower, and Paul K. Marsden. National electrical manufacturers association NU-4 performance evaluation of the PET component of the nanoPET/CT preclinical PET/CT scanner. *Journal of Nuclear Medicine*, 52:1741–1747, 11 2011.

[51] Simon R. Cherry, Ramsey D. Badawi, Joel S. Karp, William W. Moses, Pat Price, and Terry Jones. Total-body imaging: Transforming the role of positron emission tomography. *Science Translational Medicine*, 9(381):eaaf6169, 2017.

[52] Zhonghua Kuang, Xiaohui Wang, Xin Fu, Ning Ren, Qian Yang, Binqing Zhao, Chunhui Zhang, San Wu, Ziru Sang, Zhanli Hu, Junwei Du, Dong Liang, Xin Liu, Hairong Zheng, and Yongfeng Yang. Dual-ended readout small animal PET detector by using 0.5 mm pixelated LYSO crystal arrays and SiPMs. *Nuclear Instruments and Methods in Physics Research, Section A:*

Accelerators, Spectrometers, Detectors and Associated Equipment, 917:1–8, 2 2019.

[53] Mitsuo Watanabe, Akinori Saito, Takashi Isobe, Kibo Ote, Ryoko Yamada, Takahiro Moriya, and Tomohide Omura. Performance evaluation of a high-resolution brain PET scanner using four-layer MPPC DOI detectors. *Physics in Medicine and Biology*, 62:7148–7166, 8 2017.

[54] Akram Mohammadi, Fumihiko Nishikido, Naoko Inadama, Toshiaki Sakai, and Taiga Yamaya. Development of a four-layer DOI PET detector using long crystals segmented by subsurface laser engraving. *Nuclear Instruments and Methods in Physics Research, Section A: Accelerators, Spectrometers, Detectors and Associated Equipment*, 1056, 11 2023.

[55] Han Gyu Kang, Hideaki Tashima, Hidekatsu Wakizaka, Go Akamatsu, Yuma Iwao, Chie Toramatsu, and Taiga Yamaya. Development of an ultrasensitive small animal PET with 4-layer doi detectors for sub-second dynamic rodent imaging. *Physics in Medicine & Biology*, 6 2025.

[56] Willy Gsell, Cesar Molinos, Carlos Correcher, Sarah Belderbos, Jens Wouters, Sven Junge, Michael Heidenreich, Greetje Vande Velde, Ahmadreza Rezaei, Johan, Christopher Cawthorne, Frederik Cleeren, Lise Nannan, Christophe M. Deroose, Uwe Himmelreich, and Antonio J. Gonzalez. Characterization of a preclinical PET insert in a 7 tesla mri scanner: Beyond nema testing. *Physics in Medicine and Biology*, 65, 12 2020.

[57] X. Zhang, M. Niu, Y. Zhao, Q. Liang, S. Liu, W. Huang, H. Yang, X. Zhao, S. Huang, Z. Chen, Z. Deng, and Z. Gu. Development of a 256-to-4 signal multiplexing readout for high resolution PET detectors. In *2024 IEEE Nuclear Science Symposium (NSS), Medical Imaging Conference (MIC) and Room Temperature Semiconductor Detector Conference (RTSD)*, pages 1–1, 2024.